Article

On the Lifetime Estimation of SiC Power MOSFETs for Motor Drive Applications

Carmelo Barbagallo [ID]**, Santi Agatino Rizzo** *[ID]**, Giacomo Scelba, Giuseppe Scarcella and Mario Cacciato**

Department of Electrical, Electronics and Computer Engineering, University of Catania, 95129 Catania, Italy; carmelo.barbagallo@unict.it (C.B.); giacomo.scelba@unict.it (G.S.); giuseppe.scarcella@unict.it (G.S.); mario.cacciato@unict.it (M.C.)
* Correspondence: santi.rizzo@unict.it; Tel.: +39-095-738-2308

Abstract: This work presents a step-by-step procedure to estimate the lifetime of discrete SiC power MOSFETs equipping three-phase inverters of electric drives. The stress of each power device when it is subjected to thermal jumps from a few degrees up to about 80 °C was analyzed, starting from the computation of the average power losses and the commitment of the electric drive. A customizable mission profile was considered where, by accounting the working conditions of the drive, the corresponding average power losses and junction temperatures of the SiC MOSFETs composing the inverter can be computed. The tool exploits the Coffin–Manson theory, rainflow counting, and Miner's rule for the lifetime estimation of the semiconductor power devices. Different operating scenarios were investigated, underlying their impact on the lifetime of SiC MOSFETs devices. The lifetime estimation procedure was realized with the main goal of keeping limited computational efforts, while providing an effective evaluation of the thermal effects. The method enables us to set up any generic mission profile from the electric drive model. This gives us the possibility to compare several operating scenario of the drive and predict the worse operating conditions for power devices. Finally, although the lifetime estimation tool was applied to SiC power MOSFET devices for a general-purpose application, it can be extended to any type of power switch technology.

Keywords: AC motor drive; junction temperature; lifetime prediction; power MOSFET; loss modeling; reliability; SiC MOSFET

1. Introduction

The remarkable properties of silicon carbide (SiC) have made it a perfect candidate for replacing silicon-based power electronic devices in high power, high-temperature applications. In fact, SiC MOSFET technology provides excellent performance to MOSFET power devices in terms of low on-state resistance, high switching frequency, high breakdown voltage, high current capability also at very high temperature. Therefore, this technology represents a valid alternative to typical Si MOSFET and IGBT power devices for many applications [1]. The prospects for strong growth in SiC devices are high and are even stimulated by the increasing sales of plug-in hybrid and electric vehicles. Compared to the well mature Si technology, the field reliability of SiC devices must be demonstrated for various applications, and a voltage-derating design guideline needs to be established. This is especially important for applications in which reliability is extremely critical, such as the automotive and aerospace applications. Hence, it becomes imperative to apply in-depth studies on the SiC devices performance and operating limits, especially when they are used in very critical applications, for instance when they are integrated into three-phase traction inverters powering electric motors. In fact, because power conversion systems equipped with a SiC device potentially provide higher current density than one with Si devices, which leads to a larger thermal ripple, they need more stringent requirements for the package materials.

Studies on the state-of-the-art SiC MOSFET's reliability evaluation and failure mode analysis were carried out in [2–4]; these studies pointed out the evolution and improvements as well as the future challenges of this promising device technology. The electro-thermal co-simulation approach based on a PSpice-based model, including temperature dependency and a Simulink-based thermal network, was even proposed in [5] for SiC MOSFETs. Some model quantities have been obtained by FEM simulation for more accurate results, and a MATLAB script has been used to manage and interface the data from the different simulation tools. An accelerated power cycling test platform using a current source converter for SiC-MOSFET power modules was also presented in [6], where the junction temperature variations of the devices were monitored without the removal of silicone gel. Moreover, the analysis was used to examine some failure precursors and then to estimate the useful lifetime of SiC MOSFET modules. A comparison in the area of device reliability accounting for condition monitoring and active thermal control as well as the lifetime was recently carried out [7]. A method to obtain the thermal impedance of a SiC module by combining optical measurement and multi-physics simulations was proposed in [8], where the measurement of the junction temperature was performed by using fiber optic instead of temperature-sensitive electrical parameters. Several major achievements and novel architectures in SiC modules packaging were analyzed in [9], where the authors reported an accurate survey of the materials by considering their coefficient of thermal expansion and their proper combination to reduce the thermal stress in the material interfaces. The impact of different pulse width modulation control techniques on the power losses and thermal stress on SiC power modules used in a three-phase inverter was investigated in [10]. The advantages and problems due to the use of SiC MOSFET in a traction inverter were discussed in [11] to provide the guidelines for a viable solution. Electrical and thermal issues, safety and reliability problems, and challenges due to device paralleling and layout were analyzed by exploiting on-field experience in the industry sector, i.e., experimental tests, finite element analysis, and circuit simulations.

To reduce the total design and maintenance cost and to guarantee the service continuity as well as the human safety, it is also required to have an accurate prediction of the remaining lifetime prediction of power converters, which can help to prevent unwanted failures and generate better maintenance plans. While the reliability and lifetime prediction of silicon (Si) semiconductor device based power converters have been widely investigated in the literature [12–14], SiC MOSFETs are facing new reliability challenges. Hence, the design of more reliable SiC power converters requires an accurate lifetime prediction as well as online monitoring strategies for real-time lifetime prediction [15]. Different approaches can be applied to estimate the lifetime of the SiC power devices and power converters [16].

In the context discussed so far, this work presents a lifetime prediction method of SiC power MOSFETs integrated into three-phase inverters supplying a three-phase induction machine. The analysis exploits a suitable developed simulation tool realized in MATLAB and Simulink to keep the computational burden low, and it also provides a modular structure of the proposed procedure. The electric drive, the Coffin–Manson relation, the rainflow counting method, and Miner's rule are suitable for the analysis and are combined to calculate the lifetime prediction [17–28]. As it is simple and reliable, Miner's rule is the most widely used fatigue life prediction technique in this field.

In the proposed approach, the off-line prediction of the lifetime is performed, starting from the data obtained, by exploiting suitable modeling of the electric drive, operating at the conditions provided by the mission profile (MP) of the application. In the investigated case, several tests are carried out using 650 V, 45 A SiC power MOSFETs by customizing the MPs with suitable weights based on the operating conditions. Hence, the proposed procedure allows for the prediction of the behavior of the thermal stresses affecting the power switches in a wide operating range. Moreover, the option of creating several customized MPs allows us to quickly carry out many analyses and then making a comparison among them. In the

following, a step-by-step description of the developed activity is provided, along with the underlying advantages and limits of the approach.

2. Framework of the MATLAB-Simulink Tool for SiC MOSFET Lifetime Estimation

The tool provides a lifetime estimation by performing the main steps summarized in Figure 1 and listed below:

1. Simulation of the motor drive to carry out the necessary electrical quantities required to compute the power losses calculation in semiconductor power devices is described as follows: I_{on}, ma_n, $cos(\varphi)_n$, and fe_n, where the parameters I_{on}, ma_n, $cos(\varphi)_n$, and fe_n represent the maximum output current of one phase of the inverter (I_{on}) (considering a balanced three-phase system); the amplitude modulation index (ma_n); the power factor ($cos(\varphi)_n$); and the output electrical frequency (fe_n). All quantities are evaluated at steady-state conditions.
2. The temporal weight assignment is decided here, as well as the grouping of the motor drive operating conditions.
3. Power losses calculation is performed by considering the inverter driven by a space vector pulse width modulation (SVPWM) strategy. The average value of the dissipated power is computed at each switching period of the carrier signal.
4. Junction temperature estimation is performed by using a thermal Foster network, where the power losses represent the inputs of the thermal network.
5. The rainflow counting theory is applied to the junction temperature profiles obtained from the previous step to determine the number of cycles N_c associated with the n-th operating condition of the drive.
6. The number of cycles to failure N_f is calculated by applying the Coffin–Manson law.
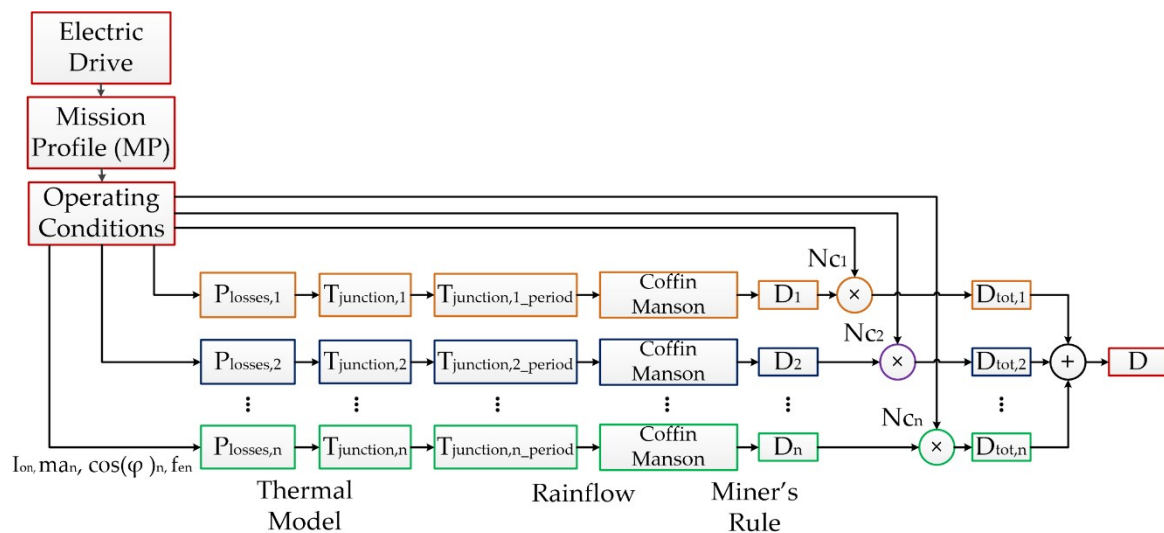7. Lifetime estimation is performed by exploiting Miner's rule.

Figure 1. Workflow of the lifetime prediction starting from the electric drive system mission profile.

### 2.1. Generation of the Mission Profile

2.1.1. Motor Drive System

The electric drive was modelled on Simulink, which is a MATLAB-based graphical programming environment and was exploited to model the entire electric drive. The model includes a three-phase asynchronous machine whose characteristics are shown in Table 1. The motor is supplied by an ideal three-phase inverter and controlled according to an indirect field oriented control (IFOC) [16]. The mission profile was carried out through the execution of a series of simulations by setting a matrix of reference speeds and reference torques values. The results of the simulations represent the dataset establishing

the operating conditions of the inverter and thus power devices, according to the considered mission profile. The Simulink model of the electric drive is shown in Figure 2. It consists of different grouped blocks: vector control IFOC, modulation block SVPWM (space vector pulse width modulation), a three-phase inverter realized with ideal power switches, and the asynchronous motor. The block "Power Factor" performs the calculation of the quantity $cos(\varphi(t))$, while the block "To Workspace" allows the average values of the modulation index $ma(t)$, the power factor $cos(\varphi)(t)$, electric frequency $f_e(t)$ and the maximum current of the phase a, $i_{as}(t)$ to be available, thus allowing us to extract the following quantities:

- $I_0 \rightarrow$ maximum value of the generic motor phase current;
- $ma_{avg} \rightarrow$ average value of the amplitude modulation index at the steady-state;
- $cos(\varphi)_{avg} \rightarrow$ average value of the power factor at steady-state;
- $f_{e\_avg} \rightarrow$ average value of the fundamental frequency at steady-state.

Table 1. Technical specification of the induction motor.

| Parameters	Symbols	Value	u.m.
Pole pairs	P	2	/
Nominal power	A_n	15	kVA
Nominal voltage	V_n	400	V
Nominal frequency	$f_{e,n}$	50	Hz
Nominal speed	n_n	1460	rpm
Stator resistance	R_s	214.7	mΩ
Stator leakage inductance	L_{ls}	991	μH
Equivalent rotor resistance	R'_r	220.5	mΩ
Equivalent rotor leakage inductance	L'_{lr}	991	μH
Mutual inductance	L_m	64.19	mH
Inertia coefficient	J	0.102	kg·m^2
Friction coefficient	F	0.009541	N·m·s
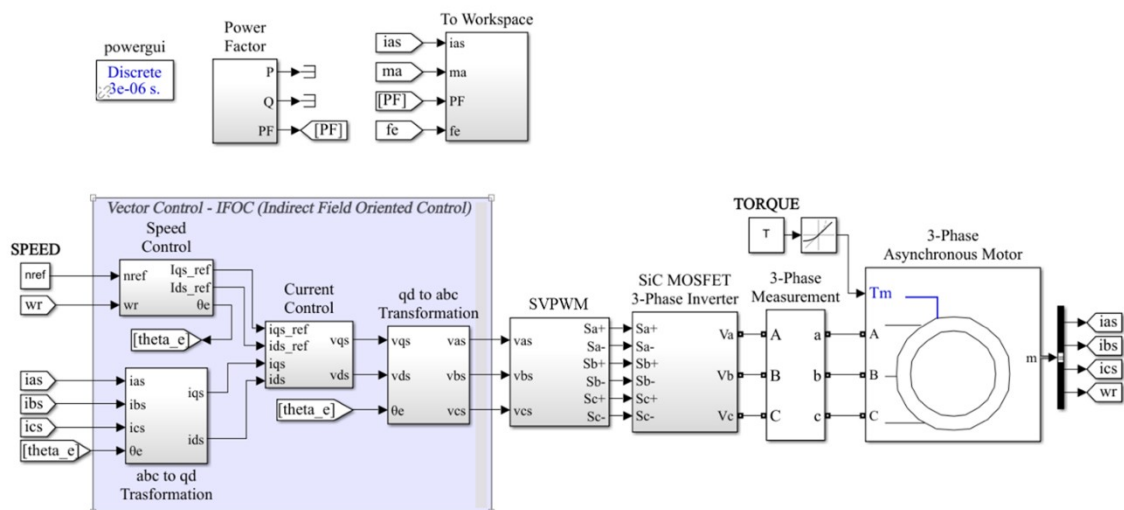
**Figure 2.** Simulink model of the electric drive system.

The simulations were carried out by using a sampling time $T_s = 3 \times 10^{-6}$ s, an input dc voltage of the inverter $V_{dc} = 560$ V, and a switching frequency of the power switches equal to $f_{sw} = 10$ kHz.

Figure 3 shows some of the results carried out from these simulations. In particular, it displays the waveforms of the above-listed electrical quantities when the reference speed and reference torque of the drive are 1400 rpm and 80 Nm, respectively. The blue traces represent the instantaneous values, while the orange traces represent the steady-state values. A campaign of simulations in which the speed is varied from 0 to 1400 rpm and

the torque from 0 to 80 Nm was executed, allowing us to identify the variation ranges of the electrical quantities, which are summarized in the surfaces shown in Figure 4. These surfaces represent the input dataset required in the next step.

(a)

(b)

(c)

(d)
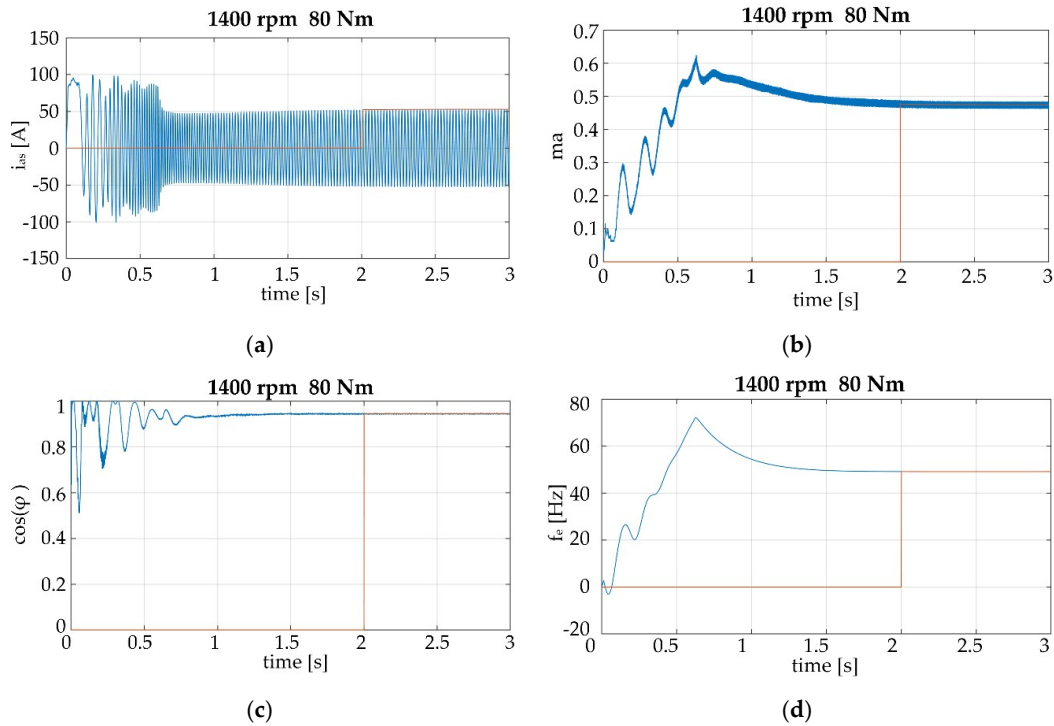
Figure 3. Results of the electric drive model operated at 1400 rpm and 80 Nm: (**a**) motor phase current a; (**b**) amplitude modulation index; (**c**) power factor; (**d**) output frequency.

(a)

(b)

(c)

(d)
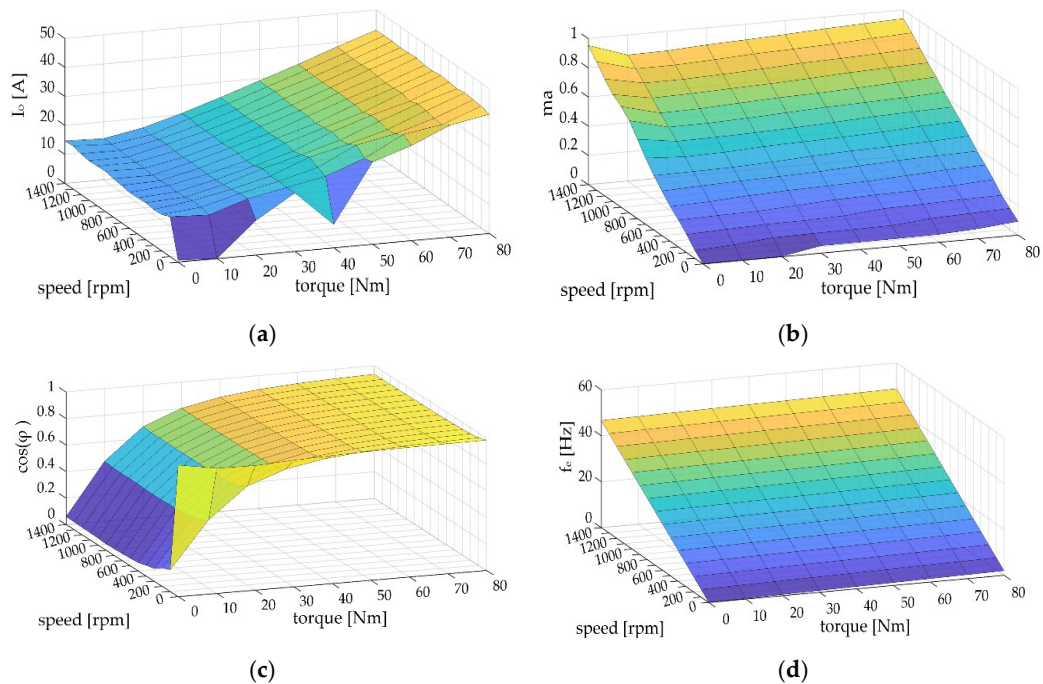
Figure 4. Results of the electric drive model as a function of the reference speed and electromagnetic torque: (**a**) maximum current; (**b**) amplitude modulation index; (**c**) power factor; (**d**) frequency.

2.1.2. Weights Assignment

For each operating condition, expressed in terms of speed and torque, a unique set of current, modulation index, power factor, and frequency values were obtained. A customizable MP, i.e., related to a specific use of the electric drive, can be obtained by assigning a time interval to each operating condition, according to a preset probability of occurrence. In this study, the sum of gaussian distributions, given by Equation (1), was used to achieve a customized time interval weights distribution, and was normalized so that their sum is equal to 100%.

$$f(x, y) = \sum_{i=1}^{n} A_i \cdot exp \left[- \left(\frac{(x - x_{0,i})^2}{2 \cdot \sigma_{x,i}^2} + \frac{(y - y_{0,i})^2}{2 \cdot \sigma_{x,i}^2} \right) \right] \tag{1}$$

where:

- $A_i \rightarrow$ peak amplitude of the i-th Gaussian distribution;
- $x_{0,i}$ and $y_{0,i} \rightarrow$ central values of x-axis and y-axis of the i-th Gaussian distribution;
- $\sigma_{x,i}$ and $\sigma_{y,i} \rightarrow$ standard deviation of x-axis and y-axis of the i-th distribution;
- x and $y \rightarrow$ torque and speed input vectors, respectively.

The above expression was applied to the dataset carried out in the previous step, by substituting the values of speed and torque to the quantities x and y respectively, while $x_{0,i}$ and $y_{0,i}$ are the central values of each Gaussian distribution. In practice, Equation (1) provides the sum of Gaussian surfaces, which establishes the weight that has to be assigned to each operating condition of the drive; in the proposed procedure, these surfaces were generated by using a MATLAB algorithm. Figure 5 shows two examples of distribution when the index $i = 1$ (single Gaussian distribution) and $i > 1$ (multiple Gaussian distributions).
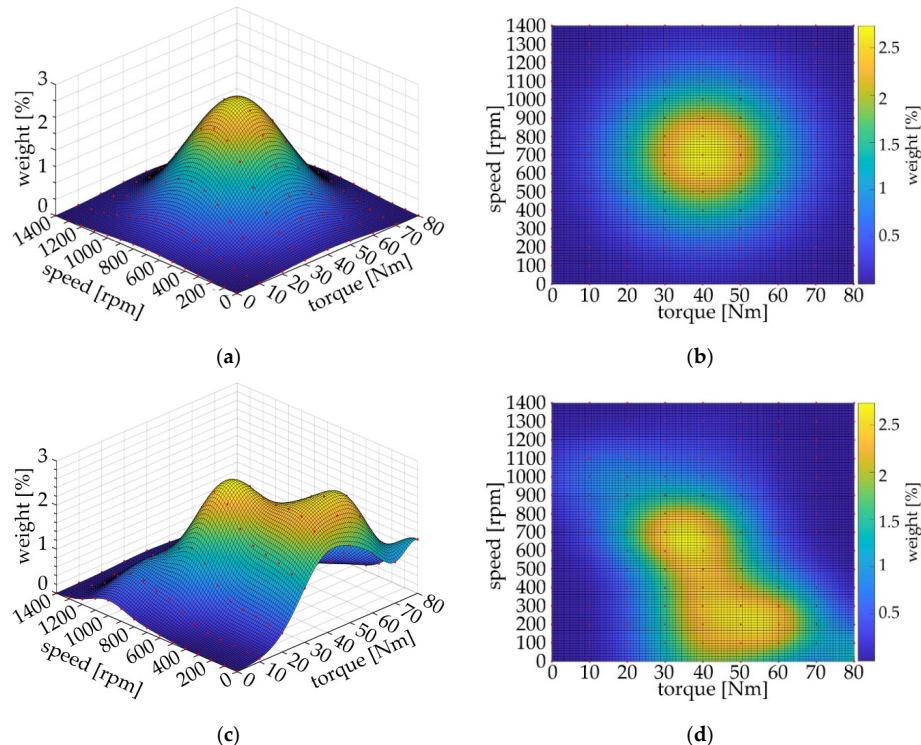
Figure 5. Examples of Gaussian surfaces: case $i = 1$ (**a**) a single Gaussian distribution "3D visualization" and (**b**) "2D visualization"; case $i > 1$ (**c**) multiple Gaussian distributions "3D visualization" and (**d**) "2D visualization".

2.1.3. Grouping of the Motor Drive Operating Conditions

After having assigned the weights to each operating condition of the drive according to the MP, a grouping process is required to group similar operating conditions, thus reducing the computational burden required to the entire lifetime estimation procedure. The grouping is performed by initially splitting in a certain number of intervals the values of I_0, ma_{avg}, $cos(\varphi)_{avg}$, f_{e_avg}, defining the minimum, maximum, step, and central value of each interval, according to Table 2. Then, the values of the electrical quantities extracted from the simulations of the electric drive are inserted in the corresponding intervals. A suitable number of intervals have to be chosen to guarantee a good compromise between the representative conditions of the drive and the computational efforts needed to compute the lifetime of the SiC power device [22,23].

Table 2. Grouping of the electric drive operating conditions.

	I_o [A]	ma	$cos(\varphi)$	f_e [Hz]
Min	0	0	0.05	0.0
Max	43.1	0.95	0.99	48.7
Step	10	0.2	0.2	10
Central value of each interval	5-15-25-35-45	0.1-0.3-0.5-0.7-0.9	0.1-0.3-0.5-0.7-0.9	5-15-25-35-45

A MATLAB function was implemented to perform the grouping procedure by assigning each working condition of the drive to a specific set data, as seen in Figure 6. All empty intervals were discarded, and they are not included in the calculation of power losses. Obviously, such an approach can be adopted even when there are data from a real MP. Even in case of handling a huge number of operating condition datasets, this mechanism enables a significant reduction of operating conditions for which the power losses have to be calculated, thus reducing the lifetime prediction time.
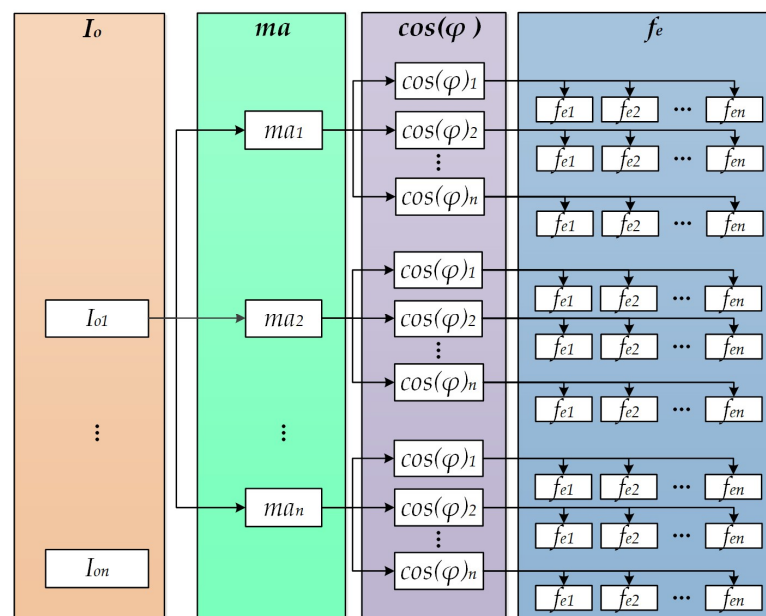
Figure 6. Grouping procedure where each motor drive operation is included in a specific subset.

2.2. SiC MOSFET Power Losses Computation

The power losses of each SiC device composing the inverter are carried out from the dataset obtained in the grouping procedure. In this analysis, the lifetime estimation is based on solder degradation, strictly correlated to the ΔT_j variations of junction temperatures in the fundamental period of the stator voltages; therefore, the calculation of the power losses

was implemented by considering the average value of the power, over each switching period T_{sw}. The following equations show the method used for the calculation [22–25]:

$$DC^n = \left\{ \begin{array}{l} DC^n_{MOS} = 0.5 \cdot [1 + m_a \cdot sin(2\pi f_e \cdot nT_{sw})] \;\; se \; 0 \le nT_{sw} < \frac{T_e}{2} \\ DC^n_{SBD} = 0.5 \cdot [1 + m_a \cdot sin(2\pi f_e \cdot nT_{sw})] \;\; se \; \frac{T_e}{2} \le nT_{sw} < T_e \end{array} \right\} \quad (2)$$

$$DC^n = \left\{ \begin{array}{l} DC^n_{MOS} = 0.5 \cdot [1 + m_a \cdot sin(2\pi f_e \cdot nT_{sw})] \;\; se \; 0 \le nT_{sw} < \frac{T_e}{2} \\ DC^n_{SBD} = 0.5 \cdot [1 + m_a \cdot sin(2\pi f_e \cdot nT_{sw})] \;\; se \; \frac{T_e}{2} \le nT_{sw} < T_e \end{array} \right\} \quad (3)$$

$$I_o^n = I_o \cdot \sin(2\pi f_e \cdot nT_{sw} - \varphi) \quad (4)$$

where:

- DC^n_{MOS}, $DC^n_{SBD} \rightarrow$ duty cycles of MOSFET and diode in the n-th switching period;
- $V^n_{on,MOS}(I_o^n)$, $V^n_{on,SBD}(I_o^n) \rightarrow$ voltage drops on MOSFET and diode in the n-th switching period;
- $E_{sw,MOS}(I_o^n)$, $E_{sw,SBD}(I_o^n) \rightarrow$ switching energy losses on MOSFET and diode in the n-th;
- f_{sw} and $T_{sw} \rightarrow$ switching frequency and switching period;
- f_e and $T_e \rightarrow$ fundamental frequency and period of the electrical quantities;
- I_o and $\varphi \rightarrow$ peak amplitude of the current and phase shift angle.

The voltage drops were carried out from the output characteristics of the SiC devices contained in the datasheets, as well as the switching energy loss and the reverse conduction characteristic. The characteristics of the SiC device under test are shown in Figure 7.

(a)

(b)

(c)

(d)
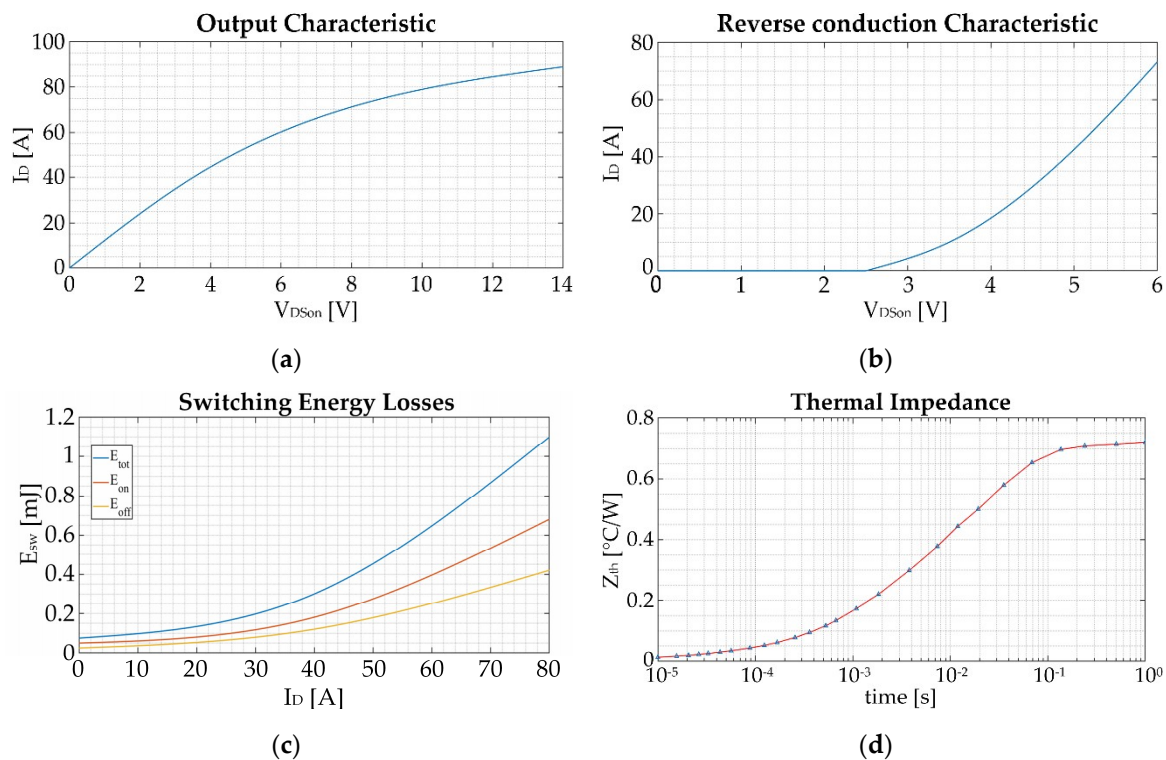
Figure 7. Technical specifications of the device under test: (**a**) output characteristic; (**b**) reverse conduction characteristic; (**c**) switching energy losses; (**d**) thermal impedance.

Figure 8 shows the power losses curve of a SiC device in a fundamental period, given for different operating conditions.
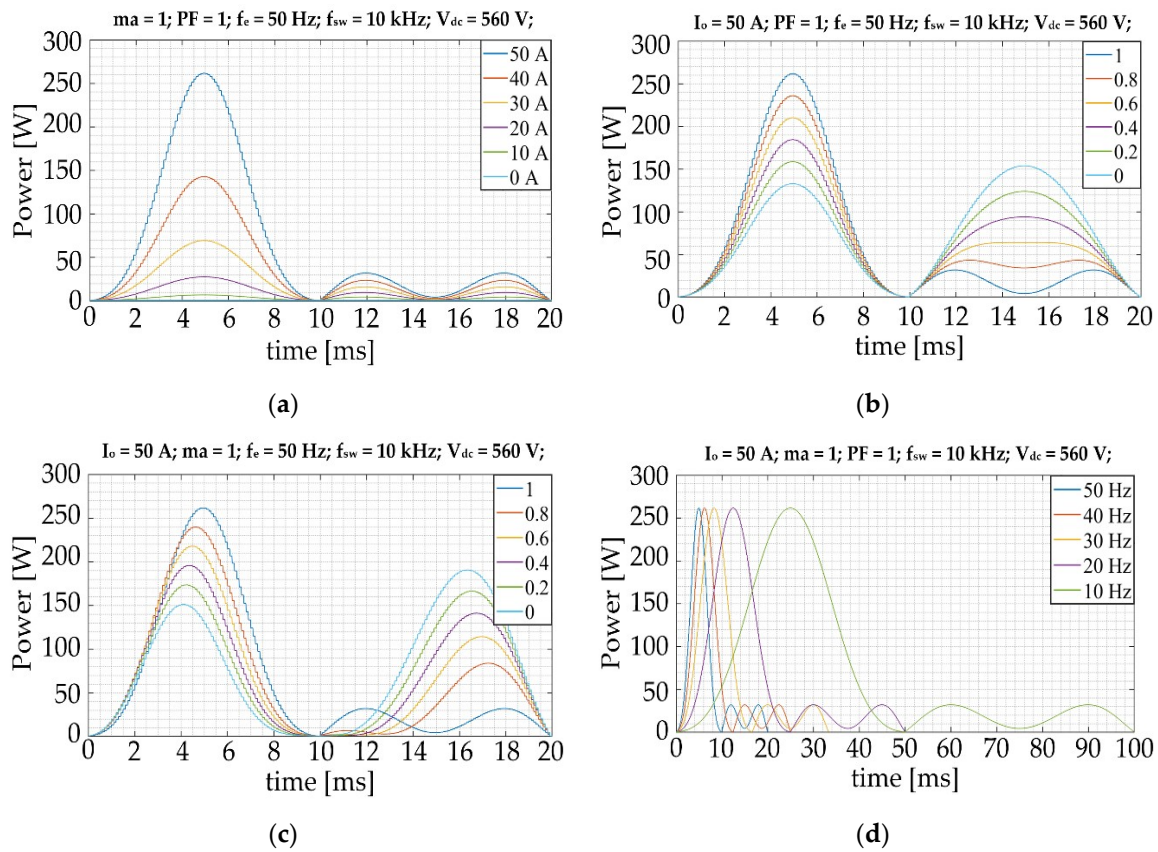
Figure 8. Power losses estimated for different operating conditions: (**a**) different currents; (**b**) different modulation indexes; (**c**) different power factors; (**d**) different fundamental frequencies.

2.3. Junction Temperature Estimation

The junction temperatures of the SiC Mosfets under test were estimated by exploiting a linear thermal model, whose generalized mathematical representation is given by [26]:

$$
\begin{bmatrix}
T_j^1(t) \\
T_j^2(t) \\
T_j^3(t) \\
\vdots \\
T_j^n(t)
\end{bmatrix}
=
\begin{bmatrix}
Z_{th}^{11}(t) & Z_{th}^{21}(t) & \cdots & Z_{th}^{n1}(t) \\
Z_{th}^{12}(t) & Z_{th}^{22}(t) & \cdots & Z_{th}^{n2}(t) \\
Z_{th}^{13}(t) & Z_{th}^{23}(t) & \cdots & Z_{th}^{n3}(t) \\
\cdots & \cdots & \cdots & \cdots \\
Z_{th}^{1n}(t) & Z_{th}^{2n}(t) & \cdots & Z_{th}^{nn}(t)
\end{bmatrix}
\begin{bmatrix}
P_1(t) \\
P_2(t) \\
P_3(t) \\
\vdots \\
P_n(t)
\end{bmatrix}
+ [T_a(t)]
\tag{5}
$$

where:

- $T_j(t) \rightarrow$ junction temperature;
- $Z_{th}(t) \rightarrow$ thermal impedance (see Figure 7d);
- $P(t) \rightarrow$ dissipated power;
- $T_a \rightarrow$ ambient temperature.

Given that in this analysis we are considering discrete SiC power devices, the thermal coupling with other devices can be assumed to be negligible, and thus the terms of mutual coupling can be nullified. Hence, Equation (5) can be rewritten as follows:

$$
T_j(t) = [Z_{th}(t) \cdot P(t)] + T_a(t)
\tag{6}
$$

According to Equation (6), the computation of the junction temperature $T_j(t)$ requires the knowledge of the thermal impedances $Z_{th}(t)$. The last is graphically provided in the datasheet of the power switch, but a circuital representation of $Z_{th}(t)$ is required to easily

simulate variable power losses profiles. This goal is reached by combining a curve-fitting procedure followed by the implementation of an equivalent Foster thermal network, as intently described in the following step.
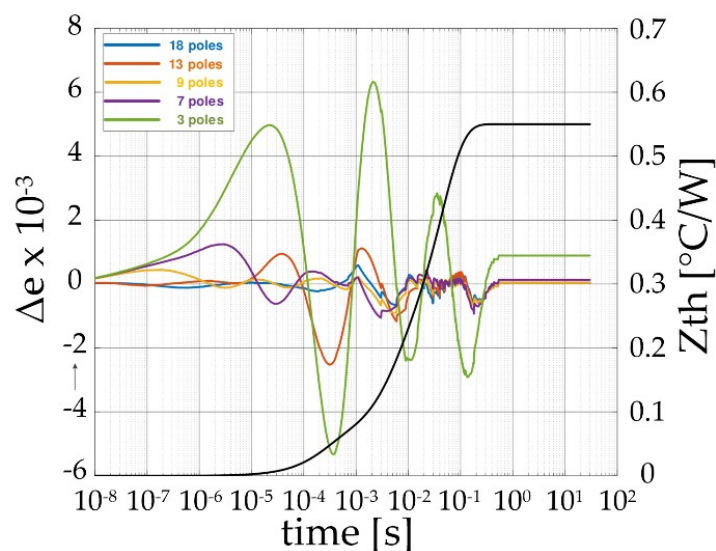
2.3.1. Curve Fitting

Starting from the thermal impedance profile $Z_{th}(t)$, it is possible to implement a curve-fitting procedure on it by using Equation (7), where it is assumed to achieve a profile of $Z_{th}(t)$ with a Foster thermal network, whose parameters $R_{th,n}$ and $C_{th,n}$ constitute the n-th pole of the network [26,27].

$$
\begin{cases}
Z_{th}(t) = \sum_{n=1}^{N_p} R_{th,n} \cdot \left(1 - e^{-\frac{t}{\tau_n}} \right) \\
\tau_n = R_{th,n} \cdot C_{th,n}
\end{cases}
\tag{7}
$$

where:

- $R_{th,n} \rightarrow$ resistance value of the n-th pole;
- $C_{th} \rightarrow$ capacitance value of the n-th pole;
- $\tau_n \rightarrow$ dissipated power;
- $T_a \rightarrow$ ambient temperature;
- $N_p \rightarrow$ number of poles.

It is important to underline the choice of the number of poles. A low number of poles does not guarantee the necessary accuracy, while a high number of poles will certainly be more accurate but results in an increase of the computational efforts. By applying the curve fitting algorithm to the SiC devices under tests, the best compromise has been obtained with seven poles, as shown in Figure 9.

Figure 9. Comparison of curve fitting using a different number of poles.

2.3.2. Foster Network

The Foster network can be realized starting from the $R_{th,n}$ and $C_{th,n}$ parameters obtained from the previous step, reproducing the thermal behavior of the device under test. Figure 10 displays the Foster network realized to emulate the $Z_{th}(t)$ of Figure 7d.
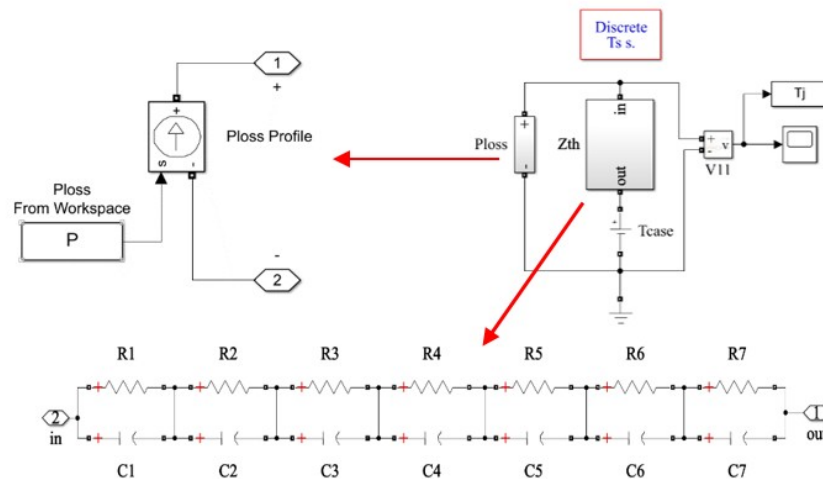
Figure 10. Simulink model of the Foster network.

2.3.3. Examples of Junction Temperature Profiles

Figure 11 displays the temperature trends of the die junction temperature for different motor drive operating conditions. It should be noted that a significant temperature variation can be experienced during the fundamental period of the phase motor current, leading to high thermal stresses. Moreover, different power losses distributions can be appreciated at varying of the load conditions, which is consistent with the theoretical analysis.
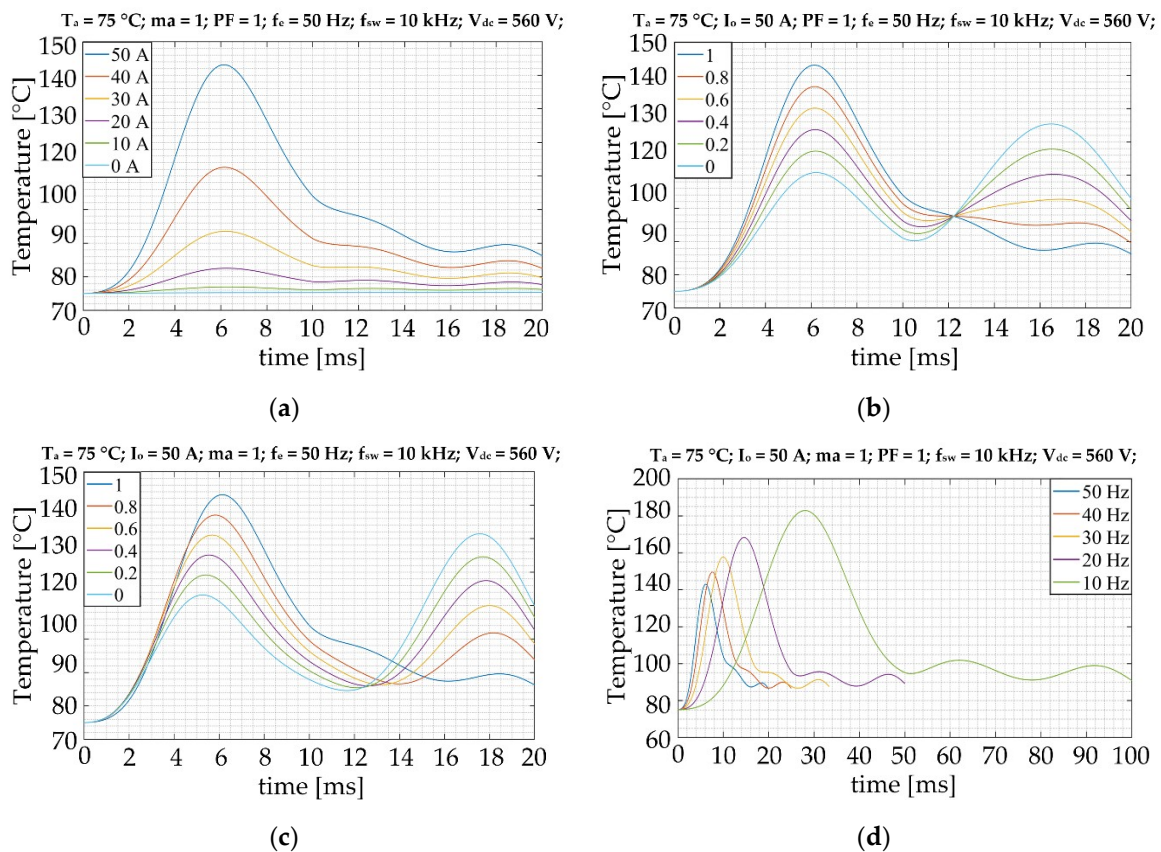

Figure 11. Temperature trends carried out for: (**a**) different currents; (**b**) different modulation indexes; (**c**) different power factors; (**d**) different fundamental frequencies.

2.4. Rainflow Counting

The rainflow-counting (or cycle counting) algorithm is used to count the number of cycles present in a generic waveform. It is a statistical method for the analysis of the random load process, and its counting principle is carried out based on the stress-deformation behavior of the material, as shown in Figure 12. It combines load reversals by defining hysteresis cycles. Each of them has a range of deformation and average stress that can be compared with the constant amplitude.

(**a**)

(**b**)

(**c**)
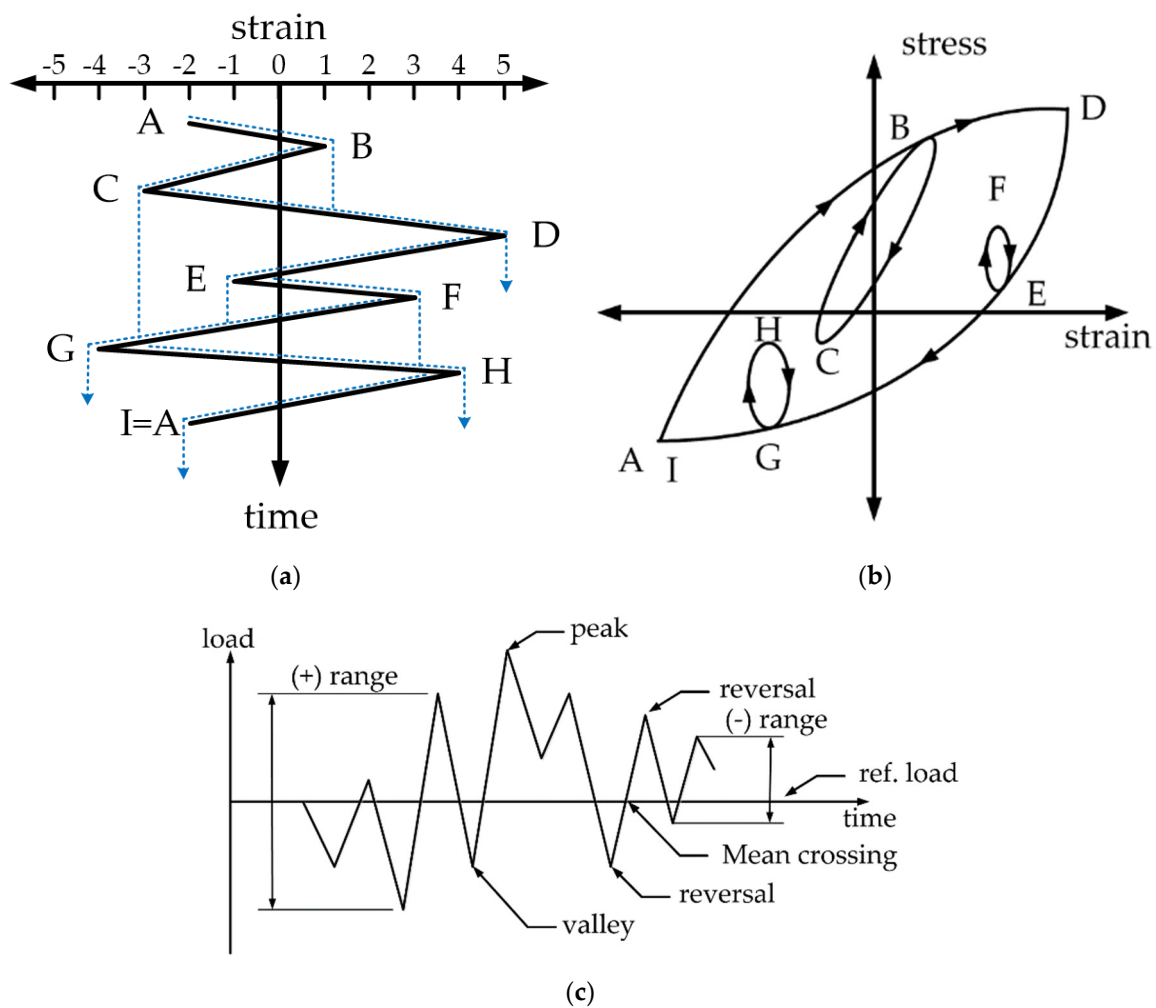
Figure 12. Graphical representation of the rainflow method: (**a**) rainflow on a load profile; (**b**) stress–strain chart; (**c**) main parameters of the rainflow.

The rules for the rainflow counting method are the following: Let X be the range taken into consideration; let Y be the previous range, adjacent to X; let S be the starting point in the history of the load profile [17,18,28]:

1. Read the next peak or valley. If the data are not available, go to step 6.
2. If there are less than three peaks and/or valleys (i.e., A, B, C of Figure 12), go to step 1. Form the X and Y ranges using the three most recent peaks and valleys that have not been discarded.
3. Compare the absolute values of the X and Y ranges:
    a. If X <Y, go to step 1.
    b. If X ≥ Y, go to step 4.
4. If range Y contains starting point S, go to step 5. Otherwise, count range Y as a cycle, discard the peak and valley of Y and go to step 2.

5. Count the Y interval as a half cycle, discard the first point (peak or valley) of the Y range, move the starting point to the second point in the Y interval, and go to step 2.
6. Count any range that was not previously counted as a half cycle.

Figure 12 summarizes the rainflow counting procedure.

The load history of Figure 12a is used to illustrate the process. Details of the cycle counting are as follows [28]:

1. S = A; Y = |A–B|; X = |B–C|; X > Y. Y contains S, that is, point A. Count |A–B| as one-half cycle and discard point A; S = B.
2. Y = |B–C|; X = |C–D|; X > Y. Y contains S, that is, point B. Count |B–C| as one-half cycle and discard point B; S = C.
3. Y = |C–D|; X = |D–E|; X < Y.
4. Y = |D–E|; X = |E–F|; X < Y.
5. Y = |E–F|; X = |F–G|; X > Y. Count |E-F| as one cycle and discard points E and F (note that a cycle is formed by pairing range E-F and a portion of range F-G).
6. Y = |C–D|; X = |D–G|; X > Y; Y contains S, that is, point C. Count |C-D| as one-half cycle and discard point C. S = D.
7. Y = |D–G|; X = |G–H|; X < Y.
8. Y = |G–H|; X = |H–I|; X < Y. End of data.
9. Count |D–G| as one-half cycle, |G–H| as one-half cycle, and |H–I| as one-half cycle.
10. End of counting (see Table 3 for a summary of the cycles counted in this example).

Table 3. Example of rainflow counting referred to Figure 12a [28].

Range	Cycle Counts	Events
1	0	/
2	0	/
3	0.5	A–B
4	1.5	B–C, G–H
5	0	/
6	0.5	H–I
7	0	/
8	1.0	C–D, G–H
9	0.5	D–G
10	0	/

After having satisfied the criterion for counting cycles N_c, the amplitude and the corresponding mean values of stress or strain for each cycle were calculated. A matrix with information on the cycle, mean value, and amplitude of stress or strain forming a cycle is thus created.

Example of Rainflow Counting

Figure 13 show an example of implementation of rainflow procedure on a temperature profile carried out in a specific drive operating condition, by applying the previous steps to the SiC MOSFETs under test; the temperature profile is first linearized to form peaks and valleys. The cycle count N_c is carried out by considering the jumps of the junction temperature ΔT_j and the average temperature T_m in each cycle.
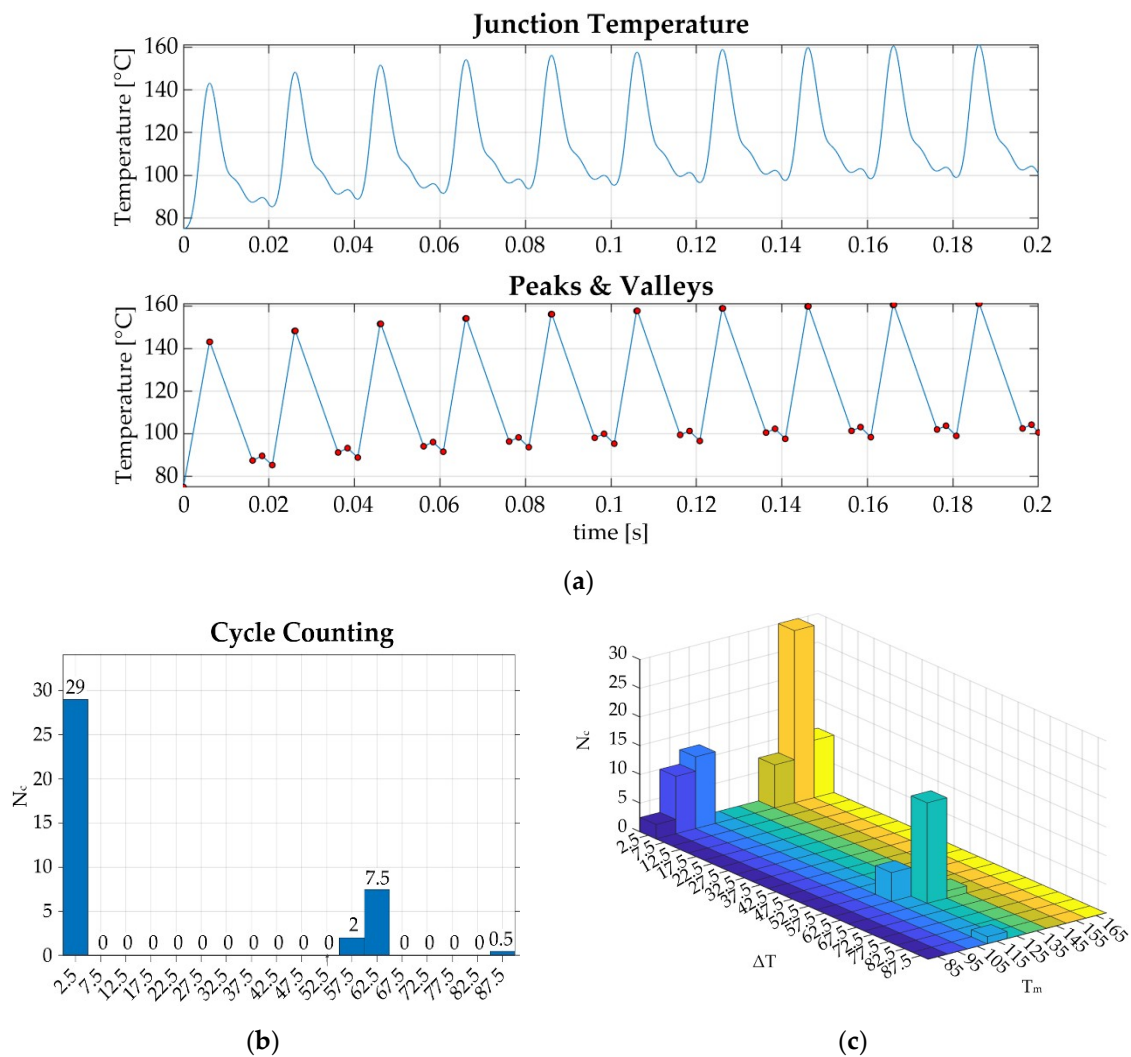
Figure 13. Example of rainflow: (**a**) linearized temperature profile in peaks and valleys; (**b**) cycle counting neglecting the average temperature; (**c**) cycle counting considering the average temperature.

2.5. Coffin–Manson's Equation

The main factors influencing the life of the power devices under test are the jumps in the junction temperature ΔT_j and the average junction temperature T_m; in fact, the estimate of the number of thermal cycles to failure N_f is based on these two parameters.

Equation (8) shows the correlation between the number of cycles to failure with thermal jumps and the average temperature of the cycles [17,19,20]

$$N_f = a \cdot \left(\Delta T_j \right)^{-n} \cdot e^{\frac{E_a}{k_B \cdot T_m}} \tag{8}$$

where:

- $N_f \rightarrow$ number of cycles to failure;
- $a \rightarrow$ experimental coefficient;
- $\Delta T_j \rightarrow$ jumps of junction temperature;
- $n \rightarrow$ experimental coefficient;
- $k_B \rightarrow$ Boltzmann constant;
- $E_a \rightarrow$ activation energy.

The parameters *a* and *n* of Equation (8) are determined according to the power cycling tests. Figure 14a shows a type of power cycling (PC_{sec}) in which an input stress is applied for a period $t_{on} < 15\ s$. In this case, the tests exert a stress in the interconnection areas close to the chips (bond wire, die-attach). On the contrary, Figure 14b shows a type of power cycling PC_{min} in which a stress is applied for a period $t_{on} > 15\ s$, stressing the solder layer. The resulting data of these tests give us information on the reliability of the devices under examination under specific operating conditions, and it is normally provided by the manufacturer [17,20,21].
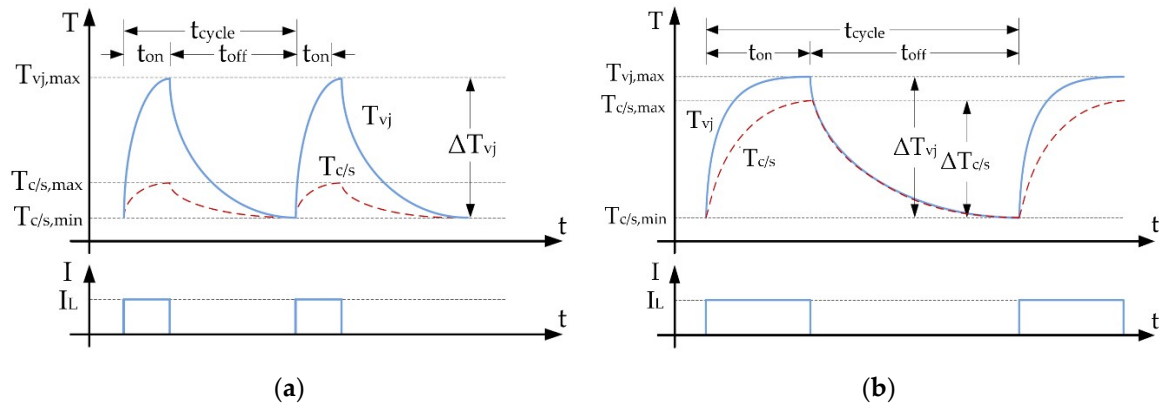

(**a**)   (**b**)

Figure 14. Types of power cycling: (**a**) fast power cycling PC_{sec}; (**b**) slow power cycling PC_{min}.

An example of Coffin–Manson curves that were calculated by considering the following parameters [20] are displayed in Figure 15.

- $a = 3.71 \times 10^{13}$
- $n = 10.122$
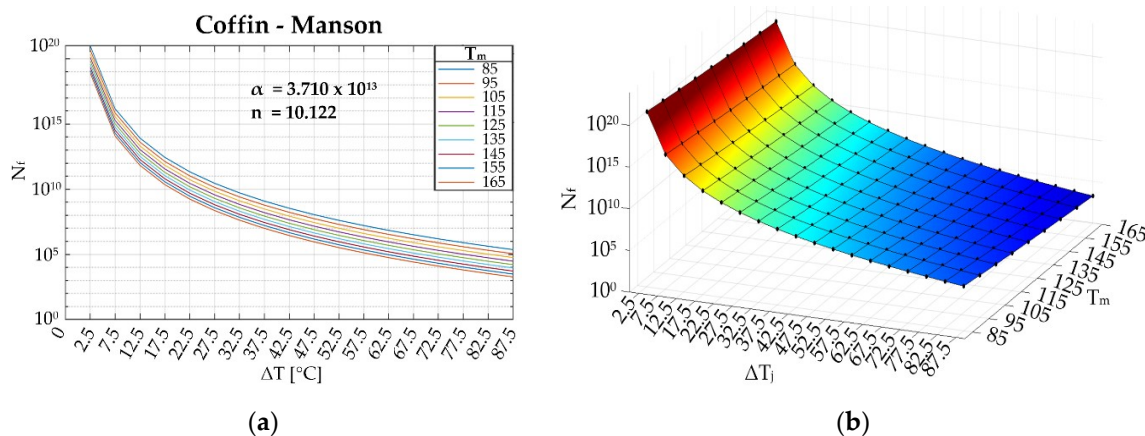- $k_B = 8.617 \times 10^{-5}\ \frac{eV}{K}$
- $E_a = 0.814$ eV

(**a**)   (**b**)

Figure 15. Coffin–Manson equation representation: (**a**) 2D curves (each one at a fixed T_m); (**b**) 3D Scheme.

2.6. Miner's Rule

The lifetime estimation is determined according to the Miner's rule, or the theory of the damage accumulation. In practice, the damage is associated with each stress condition by making the ratio between the number of thermal cycles N_c and the relative N_f associated with the same pair of ΔT_j and T_m. Extending this reasoning to all operating conditions, it is

possible to assign damage to each of them. Palmgreen–Miner's theory of linear cumulative damage, called Miner's rule, is given by [17,19,20]:

$$D = \sum_{i=1}^{k} \frac{N_{c,i}}{N_{f,i}} \tag{9}$$

$$T = \frac{1}{D} \tag{10}$$

where:

- $D \rightarrow$ total damage;
- $N_{c,i} \rightarrow$ number of cycles of the considered thermal profile associated with the *i*-th operating condition of the drive;
- $N_{f,i} \rightarrow$ number of cycles to failure associated with the specific operating condition *i*-th of the drive;
- $k \rightarrow$ total number of stresses.

By computing the $N_{c,i}/N_{f,i}$ ratios for all the *i*-th working points of the electric drive, the overall damage of SiC power devices can be predicted. If the damage is less than 1, then the power device is capable of handling the thermal stresses to which it was subjected in the entire mission profile; otherwise (if $N_{c,i}/N_{f,i}$ is greater than or equal to 1), the device is considered faulty. Parameter *T*, which would be the inverse of *D*, provides an important indication of how many cycles the device still has before failure. For "cycle", we must consider the stress input to the rainflow; in our case, one cycle corresponds to one second of junction temperature at steady-state. To obtain the lifetime, Equation (11) was used:

$$Lifetime = \sum_{i=1}^{k} \frac{1}{3600 \cdot h \cdot 365 \cdot w_i \cdot D_i} \tag{11}$$

where:

- $h \rightarrow$ hours of work per day;
- $w_i \rightarrow$ weight corresponding to the *i*-th operating condition;
- $D_i \rightarrow$ damage corresponding to the *i*-th operating condition, considering one second of junction temperature in steady-state condition;
- $k \rightarrow$ total number of stresses.

Therefore, the lifetime is estimated considering a predetermined number of hours of work per day.

3. Case Studies

In this section, the aforementioned life prediction procedure was applied to different operating scenarios for the drive so far considered: low speed–high torque, medium/high speed–low torque, and mixed operation. The goal of the following activity is to analyze the differences in lifetime estimation when different operating scenarios of the drive are considered. Figures 17, 19, and 21 show the lifetimes of each scenario as a function of daily working hours. For each scenario, daily use of the drive of 2 h is considered, although the working hours of the drive can be highly variable depending on the application.

3.1. Case Study 1: Low Speed–High Torque

This scenario is characterized by low speeds and a wide range of torques. Figure 16 shows the weight distribution considered for this mission profile, where the frequency of rotor speed is higher for values included in the range of 0–700 rpm. The conditions for which the speed is 0 rpm have a considerable weight; this could represent the numerous standing starts that normally occur in electric traction in the case of an urban cycle.
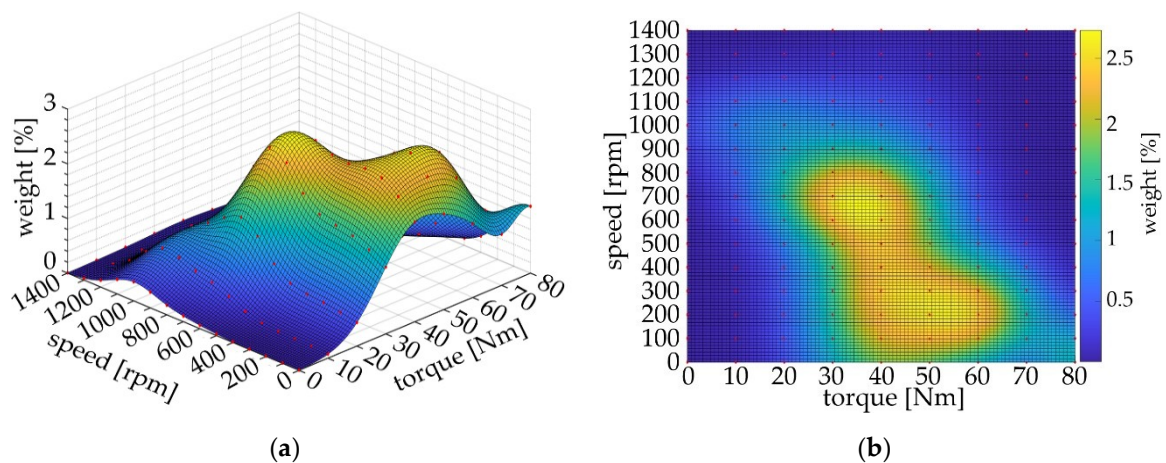
Figure 16. Weight distribution of case study 1: (**a**) 3D surface; (**b**) 2D surface.

Figure 17 shows the lifetime for this scenario, obtained by applying the step-by-step procedure defined in the previous section. Assuming an average use of the motor drive equal to 2 h per day, the lifetime of the SiC MOSFET composing the inverter of the electric drive is estimated to be about 12 years.

Figure 17. Lifetime estimation of case study 1.

3.2. Case Study 2: Medium/High Speed–Low Torque

In this scenario, the drive is mainly operated at medium-high speeds and low torques. A higher lifetime is expected because of the low torques, and thus low currents, which should lead to a lower degradation of the SiC power device under examination. Figure 18 shows the weight distribution associated to this scenario, which is projected towards medium-high speeds; in particular, a higher percentage of electric drive operation is centered around 700–800 rpm, even though the motor operation is observed up to 1400 rpm. The electromagnetic torque is normally kept quite low in this working profile, i.e., mainly around 20–30 Nm.

Figure 19 shows the lifetime estimation of case study 2. As expected, for the same hours of use, the lifetime of the SiC power MOSFET installed in the three-phase inverter is higher than in scenario 1. For instance, when an average daily use of the drive equal to 2 h is considered, the lifetime of the SiC devices is about 28 years.
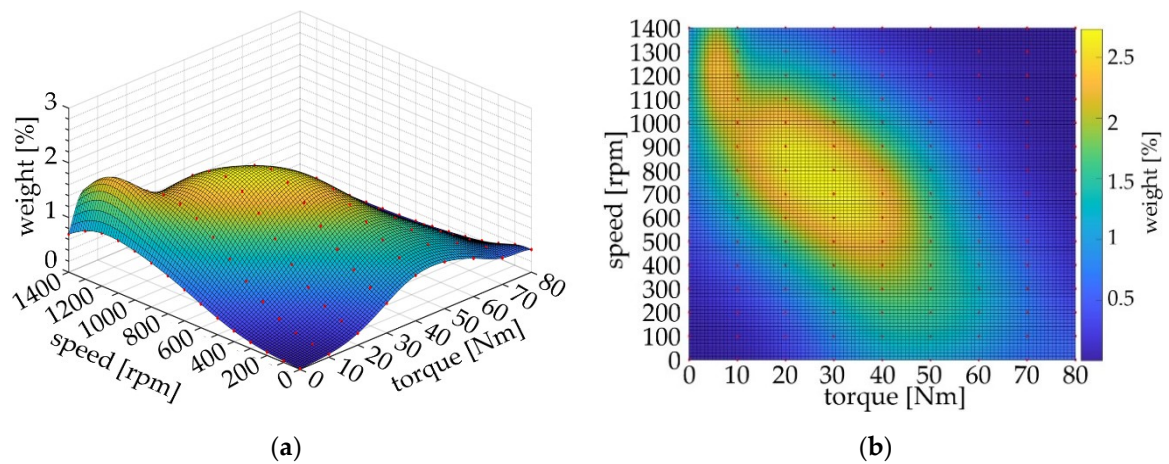
Figure 18. Weight distribution of case study 2: (**a**) 3D surface; (**b**) 2D surface.
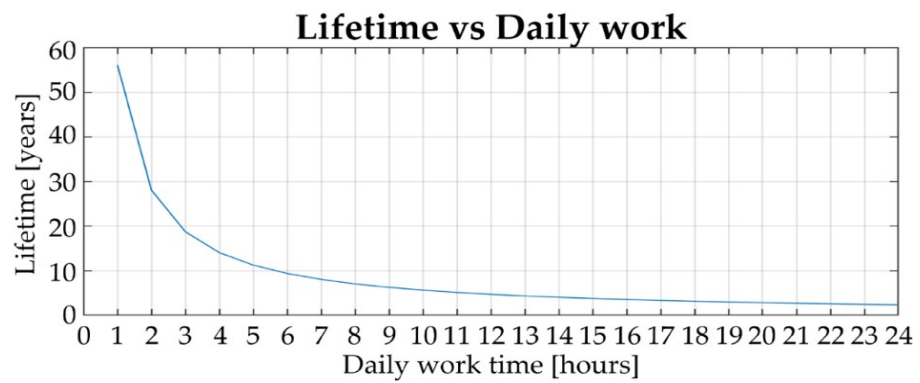

Figure 19. Lifetime estimation of case study 2.

3.3. Case Study 3: Mixed Operation

In the case of mixed-use, an intermediate situation between the two previous scenarios is considered here. The speed and torque ranges are much wider than the previous cases. Figure 20 shows the weight distribution, and it can be noted how wide the speed range is, i.e., from 200 to 1000 rpm, while the torque is mostly between 15 and 45.
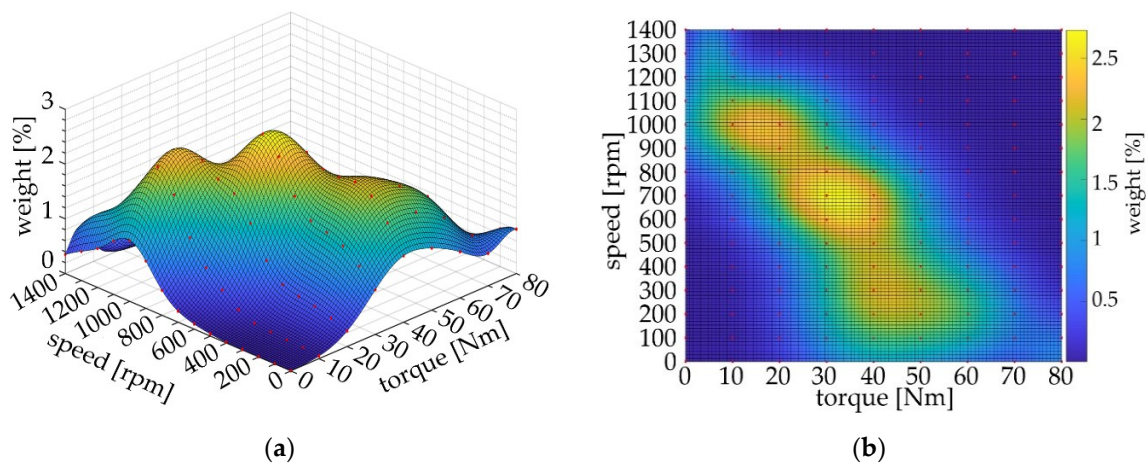

Figure 20. Weight distribution of the mixed-use: (**a**) 3D surface; (**b**) 2D surface.

Figure 21 shows the lifetime estimation of case study 3. In this case, an intermediate lifetime of previous use was found, as expected.
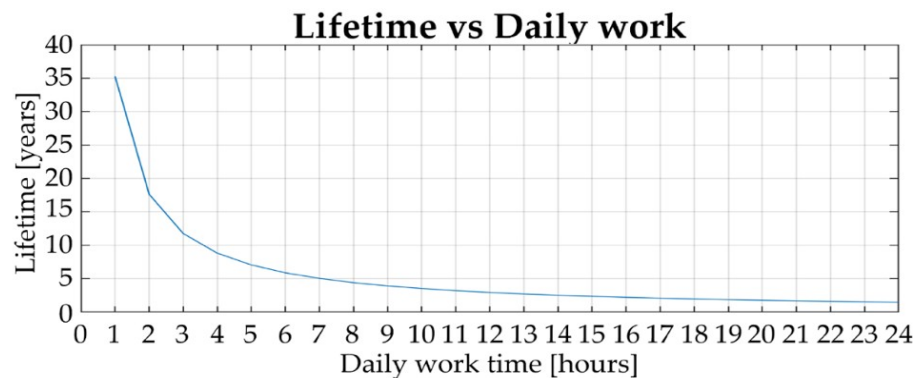

Figure 21. Lifetime estimation of mixed operation.

3.4. Results Assessment

According to the previous analysis, it is possible to note a variable lifetime that is consistent with the considered working scenarios. In fact, by assuming a daily work of the SiC-based inverter equal to 2 h, the proposed procedure provided the following lifetimes:

- Case study 1: lifetime 12 years
- Case Study 2: lifetime 28 years
- Case Study 3: lifetime 18 years

On the other hand, the same procedure allows for evaluating the number of working hours per day associated with each considered scenarios, when a lifetime equal to 15 years is imposed as a constraint for the SiC devices. The results are as follows:

- Case study 1: 1.6 h/day
- Case study 2: 2.5 h/day
- Case study 3: 3.8 h/day

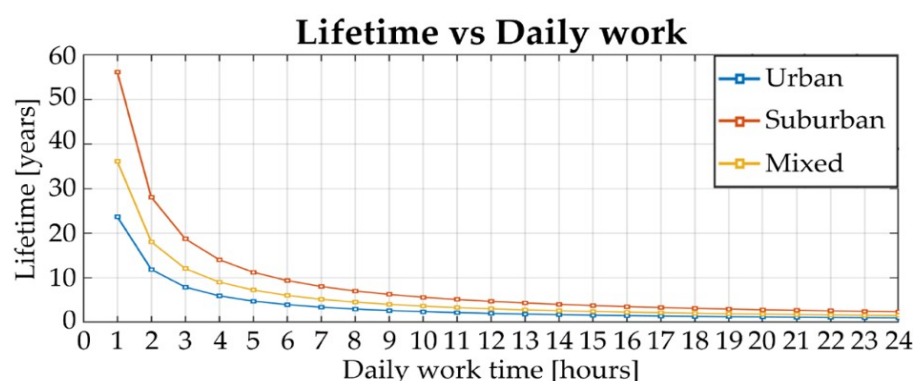Figure 22 shows the comparison between the lifetime results.

Figure 22. Comparison of the lifetime in case study 1, case study 2, and case study 3.

4. Conclusions

A detailed analysis of a lifetime estimation procedure devoted to discrete MOSFETs was presented in this paper. Such a technique was set with the aim of keeping the computational efforts and simulation times limited and low while providing an effective evaluation of thermal stresses and their effects on the power devices composing the electronic converter. The method is of a general application, and it can be used for any mission profile generated by the electric drive model. This allowed us to compare several operational states of the drive and to predict the worse operating conditions for the power devices. The

proposed approach can be extended to different operating scenarios and power devices technologies, even though the main focus of this study is the SiC technology. In the case of multi-chip modules, it is possible to easily extend the analysis also, while considering the effects of mutual thermal coupling.

Author Contributions: Conceptualization and methodology, C.B., G.S. (Giacomo Scelba) and G.S. (Giuseppe Scarcella); validation and data curation, C.B.; software and visualization C.B.; writing—original draft preparation, C.B., G.S. (Giacomo Scelba) and S.A.R.; writing—review and editing, C.B., G.S. (Giacomo Scelba), S.A.R. and M.C.; supervision, G.S. (Giuseppe Scarcella) and M.C.; project administration, G.S. (Giacomo Scelba) All authors have read and agreed to the published version of the manuscript.

Conflicts of Interest: The authors declare no conflict of interest.

References

1. Pulvirenti, M.; Montoro, G.; Nania, M.; Scollo, R.; Scelba, G.; Cacciato, M.; Scarcella, G.; Salvo, L. *2018 IEEE Energy Conversion Congress and Exposition (ECCE)*; IEEE: Portland, OR, USA, 2018; pp. 1895–1902.
2. Gonzalez, J.O.; Wu, R.; Jahdi, S.; Alatise, O. Performance and Reliability Review of 650 V and 900 V Silicon and SiC Devices: MOSFETs, Cascode JFETs and IGBTs. *IEEE Trans. Ind. Electron.* **2020**, *67*, 7375–7385. [CrossRef]
3. Zhang, L.; Yuan, X.; Wu, X.; Shi, C.; Zhang, J.; Zhang, Y. Performance Evaluation of High-Power SiC MOSFET Modules in Comparison to Si IGBT Modules. *IEEE Trans. Power Electron.* **2019**, *34*, 1181–1196. [CrossRef]
4. Ceccarelli, L.; Reigosa, P.D.; Iannuzzo, F.; Blaabjerg, F. A survey of SiC power MOSFETs short-circuit robustness and failure mode analysis. *Microelectron. Reliab.* **2017**, *76–77*, 272–276. [CrossRef]
5. Ceccarelli, L.; Bahman, A.S.; Iannuzzo, F.; Blaabjerg, F. *A Fast Electro-Thermal Co-Simulation Modeling Approach for SiC Power MOSFETs*; IEEE APEC: Portland, OR, USA, 2017.
6. Luo, H.; Iannuzzo, F.; Blaabjerg, F.; Turnaturi, M.; Mattiuzzo, E. Aging Precursors and Degradation Effects of SiCMOSFET Modules Under Highly Accelerated Power Cycling Conditions. In Proceedings of the 2017 IEEE Energy Conversion Congress and Exposition (ECCE), Cincinnati, OH, USA, 1–5 October 2017; pp. 2506–2511.
7. Nguyen, M.H.; Kwak, S. Enhance Reliability of Semiconductor Devices in Power Converters. *Electronics* **2020**, *9*, 2068. [CrossRef]
8. Kim, M.-K.; Yoon, S.W. Thermal Impedance Characterization Using Optical Measurement Assisted by Multi-Physics Simulation for Multi-Chip SiC MOSFET Module. *Micromachines* **2020**, *11*, 1060. [CrossRef] [PubMed]
9. Seal, S.; Mantooth, H.A. High Performance Silicon Carbide Power Packaging—Past Trends, Present Practices, and Future Directions. *Energies* **2017**, *10*, 341. [CrossRef]
10. Cougo, B.; Morais, L.; Segond, G.; Riva, R.; Duc, H.T. Influence of PWM Methods on Semiconductor Losses and Thermal Cycling of 15-kVA Three-Phase SiC Inverter for Aircraft Applications. *Electronics* **2020**, *9*, 620. [CrossRef]
11. Mauromicale, G.; Raciti, A.; Rizzo, S.A.; Susinni, G.; Abbatelli, L.; Buonomo, S.; Cavallaro, D.; Giuffrida, V. SiC Power Modules for Traction inverter in Automotive Application. In Proceedings of the Annual Conference of the IEEE Industrial Electronics Society, Lisbon, Portugal, 14–17 October 2019.
12. Zhou, D.; Wang, H.; Blaabjerg, F. Mission Profile Based System-Level Reliability Analysis of DC/DC Converters for a Backup Power Application. *IEEE Trans. Power Electron.* **2018**, *33*, 8030–8039. [CrossRef]
13. Khosroshahi, A.; Abapour, M.; Sabahi, M. Reliability evaluation of conventional and interleaved DC–DC boost converters. *IEEE Trans. Power Electron.* **2015**, *30*, 5821–5828. [CrossRef]
14. Ni, Z.; Lyu, X.; Yadav, O.P.; Singh, B.N.; Zheng, S.; Cao, D. Overview of Real-Time Lifetime Prediction and Extension for SiC Power Converters. *IEEE Trans. Power Electron.* **2020**, *35*, 7765–7794. [CrossRef]
15. Hirschmann, D.; Tissen, S.; Schroder, S.; De Doncker, R.W. Reliability prediction for inverters in hybrid electrical vehicles. *IEEE Trans. Power Electron.* **2007**, *22*, 2511–2517. [CrossRef]
16. Novotny, D.W.; Lipo, T.A. *Vector Control and Dynamics of AC Drives*; Oxford University Press Inc.: New York, NY, USA, 1996.
17. Wang, B.; Cai, J.; Du, X.; Zhou, E.L. Review of Power Semiconductor Device Reliability for Power Converters. *CPSS Trans. Power Electron. Appl.* **2017**, *2*, 101–117. [CrossRef]
18. Leddy, L.; Reddy, G.; Tolbert, L.M.; Ozpineci, B.; Pinto, O.P. Rainflow Algorithm-Based Lifetime Estimation of Power Semiconductors in Utility Applications. *IEEE Trans. Ind. Appl.* **2015**, *51*, 3368–3375.
19. Letor, R.; Russo, S.; Crisafulli, R. *Life Time Prediction and Design for Reliability of Smart Power Devices for Automotive Exterior Lighting*; STMicroelectronics: Catania, Italy, 2008.
20. Lai, W.; Chen, M.; Alatise, O.; Xu, S.; Mawby, P. Low ΔTj Stress Cycle Effect in IGBT Power Module Die-Attach Lifetime Modeling. *IEEE Trans. Power Electron.* **2016**, 6575–6585. [CrossRef]

21. ABB Switzerland Ltd Semiconductors. *Load-Cycling Capability of HiPak IGBT Modules*; Application Note 5SYA 2043-04; ABB Switzerland Ltd.: Lenzburg, Switzerland, 2004; pp. 1–8.
22. Ma, K.; Blaabjerg, F. Multi-Timescale Modelling for the Loading Behaviours of Power Electronics Converter. In Proceedings of the 2015 IEEE Energy Conversion Congress and Exposition (ECCE), Montreal, QC, Canada, 20–24 September 2015; pp. 5749–5756.
23. Ceccarelli, L.; Kotecha, R.M.; Bahman, A.S.; Iannuzzo, F.; Mantooth, H.A. Mission-Profile-Based Lifetime Prediction for a SiC mosfet Power Module Using a Multi-Step Condition-Mapping Simulation Strategy. *IEEE Trans. Power Electron.* **2019**, *34*, 9698–9708. [CrossRef]
24. Ahmed, M.H.; Wang, M.; Hassan, M.A.S.; Ullah, I. Power Loss Model and Efficiency Analysis of Three-Phase Inverter Based on SiC MOSFETs for PV Applications. *IEEE Access* **2019**, *7*, 75768–75781. [CrossRef]
25. Schonberger, J. Averaging Methods for Electrical-Thermal Converter Models. In Proceedings of the 2011 14th European Conference on Power Electronics and Applications, Birmingham, UK, 30 August–1 September 2011; pp. 1–8.
26. Allegra, A.; Scelba, G.; Cacciato, M.; Foti, S.; Scarcella, G.; Salerno, N.; Cavallaro, D.; Bazzano, A.; Aiello, G. *Thermal Equivalent Circuit Model of Multi-Die SiC Power Modules*; 2020 ELEKTRO: Taormina, Italy, 2020; pp. 1–6.
27. Chen, Z.; Gao, F.; Yang, C.; Peng, T.; Zhou, L.; Yang, C. *Converter Lifetime Modeling Based on Online Rainflow Counting Algorithm*; IEEE: Vancouver, BC, Canada, 2019; pp. 1743–1748.
28. ASTM American Society for Testing and Materials, Standard Practices for Cycle Counting in Fatigue Analysis. Designation: E 1049–85 (Reapproved 1997). In *Annual Book of ASTM Standards*; ASTM: West Conshohocken, PA, USA, 2014; pp. 1–10.